



# Inhibition of PIKfyve kinase prevents infection by Zaire ebolavirus and SARS-CoV-2

Yuan-Lin Kang<sup>a,b,1</sup>, Yi-ying Chou<sup>a,b,2</sup>, Paul W. Rothlauf<sup>c,d</sup>, Zhuoming Liu<sup>c</sup>, Timothy K. Soh<sup>d</sup>, David Cureton<sup>d,e</sup>, James Brett Case<sup>f</sup>, Rita E. Chen<sup>f,g</sup>, Michael S. Diamond<sup>c,f,g</sup>, Sean P. J. Whelan<sup>c,3</sup>, and Tom Kirchhausen<sup>a,b,h,3</sup>

<sup>a</sup>Department of Cell Biology, Harvard Medical School, Boston, MA 02115; <sup>b</sup>Program in Cellular and Molecular Medicine, Boston Children's Hospital, Boston, MA 02115; <sup>c</sup>Department of Molecular Microbiology, Washington University in St. Louis, St. Louis, MO 63110; <sup>d</sup>Program in Virology, Harvard Medical School, Boston, MA 02115; <sup>e</sup>Boehringer Ingelheim Animal Health, Inc. Duluth, GA 30096; <sup>f</sup>Department of Medicine, Washington University in St. Louis, St. Louis, MO 63110; <sup>g</sup>Department of Pathology & Immunology, Washington University in St. Louis, St. Louis, MO 63110; and <sup>h</sup>Department of Pediatrics, Harvard Medical School, Boston, MA 02115

Edited by Peter Palese, Icahn School of Medicine at Mount Sinai, New York, NY, and approved July 22, 2020 (received for review April 22, 2020)

**Virus entry is a multistep process. It initiates when the virus attaches to the host cell and ends when the viral contents reach the cytosol. Genetically unrelated viruses can subvert analogous subcellular mechanisms and use similar trafficking pathways for successful entry. Antiviral strategies targeting early steps of infection are therefore appealing, particularly when the probability for successful interference through a common step is highest. We describe here potent inhibitory effects on content release and infection by chimeric vesicular stomatitis virus (VSV) containing the envelope proteins of Zaire ebolavirus (VSV-ZEBOV) or severe acute respiratory syndrome coronavirus 2 (SARS-CoV-2) (VSV-SARS-CoV-2) elicited by Apilimod and Vacuolin-1, small-molecule inhibitors of the main endosomal phosphatidylinositol-3-phosphate/phosphatidylinositol 5-kinase, PIKfyve. We also describe potent inhibition of SARS-CoV-2 strain 2019-nCoV/USA-WA1/2020 by Apilimod. These results define tools for studying the intracellular trafficking of pathogens elicited by inhibition of PIKfyve kinase and suggest the potential for targeting this kinase in developing small-molecule antivirals against SARS-CoV-2.**

in cells, PI(3,5)P2 is particularly important for endomembrane homeostasis. It is produced by PI-3P-5-kinase (PIKfyve), which phosphorylates the D-5 position in phosphatidylinositol-3-phosphate (PI3P) to yield phosphatidylinositol 3,5-bisphosphate (PI(3,5)P2) (10). First cloned as mammalian p235 (11), PIKfyve is a 240-kDa class III lipid kinase, present on the cytosolic face of endosomal membranes (12, 13) as part of a ternary complex with the PI(3,5)P2 5-phosphatase Sac3 and ArPIKfyve (14).

Ablation of PIKfyve function by genetic (12, 15) or pharmacological means (16–20) causes endosomal swelling and vacuolation of late endosomes and endolysosomes. It is thought that these changes result from decreased membrane fission and concomitant interference in endosomal traffic (13, 21). Small-molecule inhibitors of PIKfyve, all of which have some structural resemblance to each other, have been studied as potential drugs for treating cancer and autoimmune diseases. These inhibitors include Apilimod (19), Vacuolin-1 (18), a series of 30 Vacuolin-related

COVID-19 | SARS-CoV-2 | ZEBOV | APILIMOD | Vacuolin-1

**M**embrane-enveloped viruses deliver their contents to cells via envelope protein-catalyzed membrane fusion. Binding of virus to specific host cell receptor(s) triggers membrane fusion, which can occur directly at the plasma membrane or following endocytic uptake. Viruses that require endocytic uptake can use different initial trafficking routes to reach the site of membrane fusion. In endosomes, acidic pH serves to trigger conformational rearrangements in the viral envelope proteins that catalyze membrane fusion, as seen for influenza A virus and vesicular stomatitis virus (VSV). For Zaire ebolavirus (ZEBOV), proteolytic processing of the envelope protein by host cell proteases (1) is necessary to expose the receptor binding domain prior to engagement of Niemann–Pick disease type 1C (NPC1 or NPC Intracellular Cholesterol Transporter 1)—the late endosomal–lysosomal receptor protein (2). Proteolytic processing is also required for severe acute respiratory syndrome coronavirus (SARS-CoV) (3, 4), and for the current pandemic SARS-CoV-2 (5). Lassa fever virus (LASV) uses a different mechanism, binding alpha-dystroglycan at the plasma membrane (6), for internalization with a subsequent pH-regulated switch that leads to engagement of lysosomal-associated membrane protein 1 for membrane fusion (7). Lymphocytic choriomeningitis virus (LCMV) also uses alpha-dystroglycan (6) and is internalized in a manner that depends on endosomal sorting complexes required for transport proteins (8), although it remains unknown whether a second receptor is required.

A hallmark of the endolysosomal system is controlled dynamic trafficking of vesicular carriers among its various subcompartments. Phosphoinositides are markers for defining the identity of these subcompartments, because they are restricted in their distribution to specific intracellular membranes (reviewed in ref. 9). Although it is one of the least abundant of the phosphoinositides

## Significance

**The membrane fusion proteins of viral pathogens as diverse in their replication strategies as coronaviruses and filoviruses depend, for their functional activity, on proteolytic processing during cell entry. Endosomal cathepsins carry out the cleavages. We have constructed chimeric forms of vesicular stomatitis virus (VSV) bearing the fusion proteins of Zaire ebolavirus (ZEBOV) or SARS coronavirus 2 (SARS-CoV-2) and shown that two small-molecule inhibitors of an endosomal lipid kinase (PIKfyve) inhibit viral infection by preventing release of the viral contents from endosomes. Both inhibitory compounds cause distension of Rab5 and Rab7 subcompartments into small vacuoles. One of them (Apilimod) also inhibits infection of cells by authentic SARS-CoV-2. The results point to possibilities for host targets of antiviral drugs.**

Author contributions: M.S.D., S.P.J.W., and T.K. designed research; Y.-L.K., Y.-y.C., P.W.R., Z.L., J.B.C., and R.E.C. performed research; Y.-L.K., Y.-y.C., T.K.S., and D.C. contributed new reagents/analytic tools; Y.-L.K. and T.K. analyzed data; T.K. wrote the paper; and T.K. supervised the project.

Competing interest statement: M.S.D. is a consultant for Inbios, Vir Biotechnology, and NGM Biopharmaceuticals, and is on the Scientific Advisory Board of Moderna. The M.S.D. laboratory at Washington University School of Medicine has received sponsored research agreements from Moderna and Emergent BioSolutions.

This article is a PNAS Direct Submission.

This open access article is distributed under [Creative Commons Attribution License 4.0 \(CC BY\)](https://creativecommons.org/licenses/by/4.0/).

<sup>1</sup>Present address: Department of Stem Cell and Regenerative Biology, Harvard University, Cambridge, MA 02138.

<sup>2</sup>Present address: Biogen, Cambridge, MA 02142.

<sup>3</sup>To whom correspondence may be addressed. Email: spjwhelan@wustl.edu or kirchhausen@crystal.harvard.edu.

This article contains supporting information online at <https://www.pnas.org/lookup/suppl/doi:10.1073/pnas.2007837117/-DCSupplemental>.

molecules (22), YM201636 (16), and WX8 chemical family members (20). Physiological effects of these compounds in cells include inhibition of autophagy (17, 22, 23), reduced generation of IL-12/IL-23 (24), and reduced dendritic cell infiltration in psoriasis (25).

Apilimod also inhibits infection by several viruses, including ZEBOV. Although it does not alter the pH of endosomes nor inhibit cathepsin B or L (26), Apilimod blocks entry of ZEBOV and other pathogenic filoviruses (27). Several groups reported that Apilimod prevents colocalization of VSV-ZEBOV pseudoviruses with the ZEBOV endosomal receptor NPC1, but does not prevent colocalization with early endosomal antigen 1 (EEA1) (5, 27, 28). Apilimod also inhibits entry of pseudotyped viruses bearing the spike proteins of Middle East respiratory syndrome CoV, SARS-CoV, and SARS-CoV-2, as well as of authentic mouse hepatitis virus particles (5).

Here, we have studied the effects of Apilimod on infection of VSV-eGFP-SARS-CoV-2 and VSV-eGFP-ZEBOV chimeras and showed that Apilimod blocks infection of both, with a concentration that inhibits response by 50% (IC<sub>50</sub>) of ~50 nM. Apilimod and Vacuolin-1 also prevented entry and infection of VSV-MeGFP-ZEBOV and many of the internalized VSV-MeGFP-ZEBOV virions colocalized with NPC1 in the distended, vacuolated endosomes. This suggests that blocking PIKfyve kinase has the same downstream effects on these viruses, even though VSV-eGFP-SARS-CoV-2 does not require interaction with NPC1 for membrane

fusion. Apilimod also inhibits infection by authentic SARS-CoV-2 strain 2019-nCoV/USA-WA1/2020 virus, with an IC<sub>50</sub> slightly lower than the IC<sub>50</sub> for the VSV-eGFP-SARS-CoV-2. We suggest that Apilimod, which has passed safety tests in previous human clinical trials for nonviral indications (24, 25, 29, 30), is a potential starting point for developing small-molecule entry inhibitors of SARS-CoV-2 that could limit infection and disease pathogenesis.

## Results

**Apilimod Inhibits Infection of VSV-MeGFP-LCMV and VSV-ZEBOV.** We inoculated SVG-A cells with VSV chimeras expressing the viral matrix protein (M) fused to eGFP (MeGFP). The chimeras include VSV (VSV-MeGFP, which initiates fusion at pH < 6.2), VSV-V269H GP (VSV-MeGFP-V269H, a variant of VSV GP that initiates fusion at pH < 5.8), rabies virus GP (VSV-MeGFP-RABV), Lassa virus GP (VSV-MeGFP-LASV), LCMV GP (VSV-MeGFP-LCMV), or Zaire ebolavirus GP (VSV-MeGFP-ZEBOV). Following the incubation protocol summarized in Fig. 1A, we tested the effects on infection of Apilimod or Vacuolin-1; both compounds are small-molecule inhibitors of PIKfyve kinase, which generates PI(5)P and PI(3,5)P<sub>2</sub> in late endosomes and lysosomes. Using a flow cytometry-based assay to monitor a single round of infection determined by expression of viral MeGFP (Fig. 1B), we found that Apilimod and Vacuolin-1

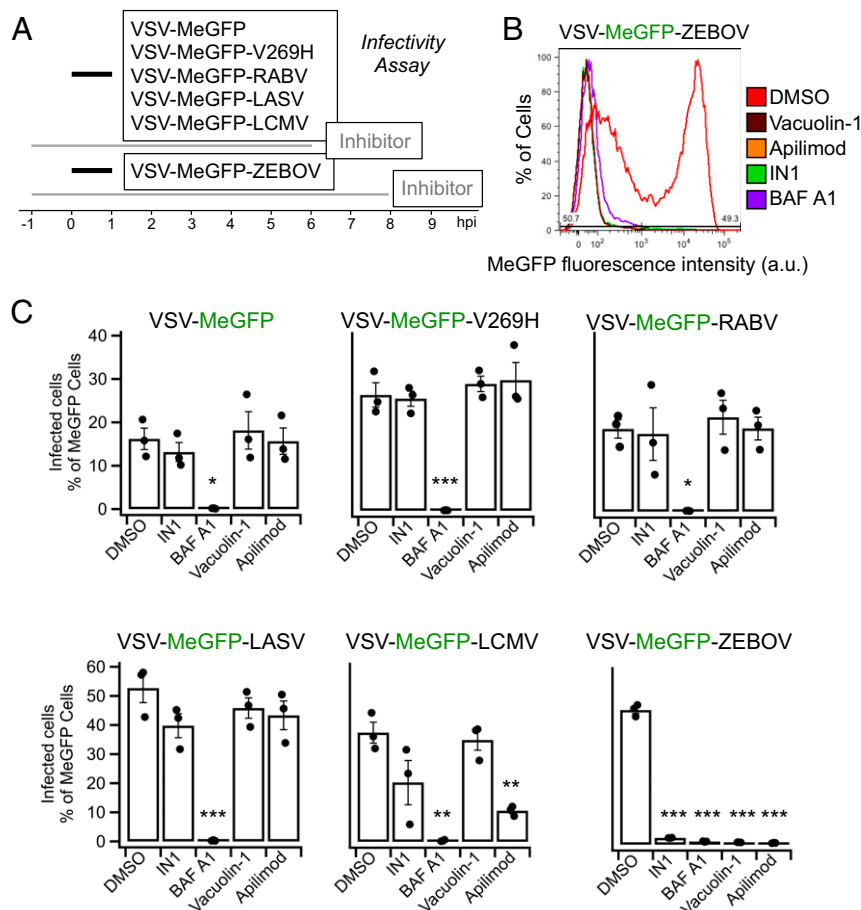


**Fig. 1.** Apilimod and Vacuolin-1 inhibit VSV-MeGFP-ZEBOV infection. (A) Schematic of infectivity assay, where SVG-A cells were pretreated for 1 h with 5  $\mu$ M Vacuolin, 5  $\mu$ M Apilimod, 5  $\mu$ M IN1, or 10 nM BAF A1 and subsequently infected with VSV-MeGFP (MOI = 2), VSV-MeGFP-V269H (MOI = 1), VSV-MeGFP-RABV (MOI = 0.6), VSV-MeGFP-LASV (MOI = 0.6), VSV-MeGFP-LCMV (MOI = 0.6), or VSV-MeGFP-ZEBOV (MOI = 0.6) for 1 h in the presence of drugs. The cells were then washed to remove unbound virus and incubated for the indicated times in the presence of drugs. The cells were then fixed, and the percentage of cells expressing viral MeGFP was measured by flow cytometry. (B) Representative flow cytometry results of an infection assay using VSV-MeGFP-ZEBOV. (C) Quantification of the infectivity is shown with averages from three independent experiments per condition, each determined as a duplicate measurement (error bars show SEM). The statistical significance was determined using a one-way ANOVA and Tukey post hoc test (\* $P \leq 0.05$ ; \*\* $P \leq 0.01$ ; \*\*\* $P \leq 0.001$ ).

potently inhibit VSV-MeGFP-ZEBOV infection (Fig. 1C). These results agree with results obtained by others with Apilimod (26, 31) in different cell types infected with murine leukemia virus (MLV) virus pseudotyped with ZEBOV GP or with Ebola virus itself (26, 27, 32). Apilimod was a less effective inhibitor of VSV-MeGFP-LCMV infection, and Vacuolin-1 had no effect at the concentration used. In contrast, Apilimod and Vacuolin-1 failed to prevent infection by VSV-MeGFP, VSV-MeGFP-V269H, VSV-MeGFP-RABV, or VSV-MeGFP-LASV (Fig. 1C). IN1 (33), an inhibitor of the phosphoinositide kinase

Vps34, the main endosomal generator of PI3P, also interfered with VSV-MeGFP-LCMV and VSV-MeGFP-ZEBOV infection (Fig. 1C). All of these viruses require low pH to trigger viral membrane fusion with the endosomal membranes, and, as expected, infection was fully blocked by Bafilomycin A1, which inhibits the vacuolar type  $H^+$ -ATPase (V-ATPase) acidification activity (Fig. 1C).

**Apilimod and Vacuolin-1 Prevent Cytoplasmic Entry of VSV-MeGFP-ZEBOV.** Productive infection requires delivery of the viral ribonucleoprotein core (RNP) into the cytosol. In these

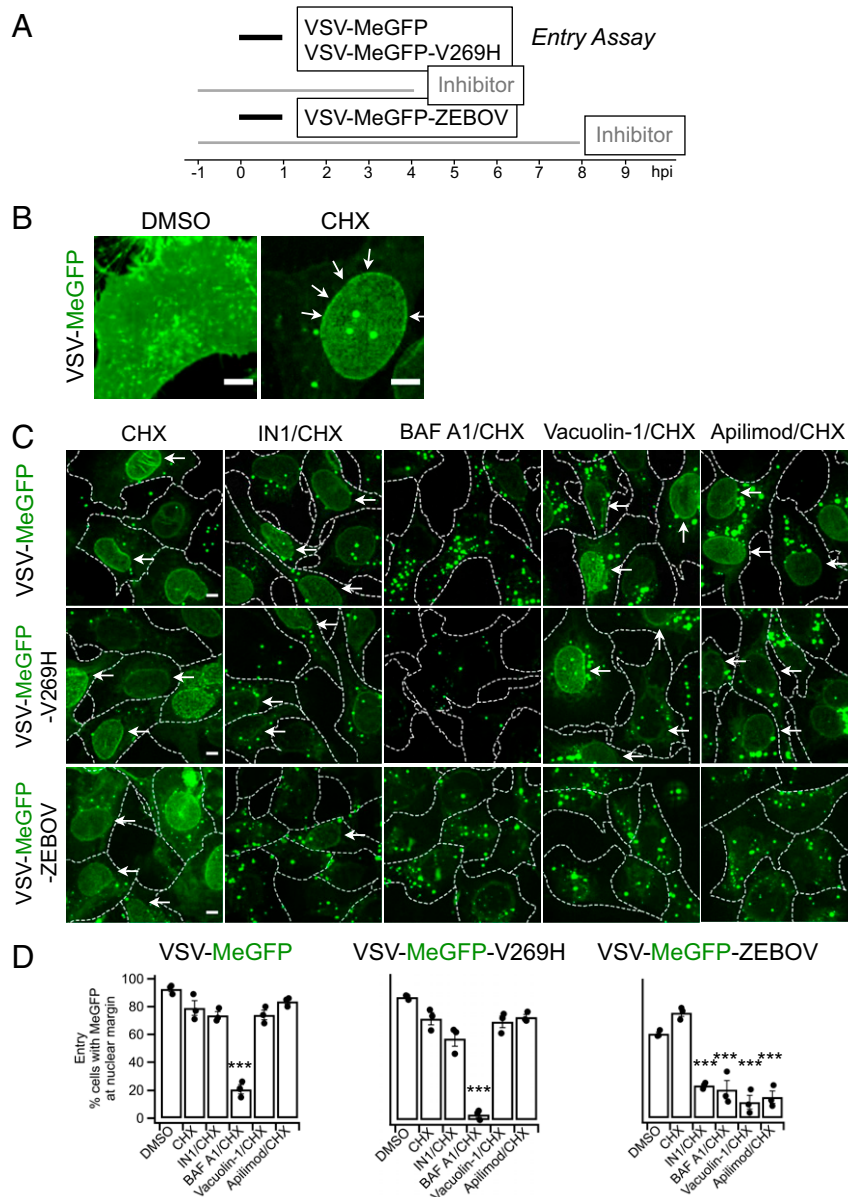


**Fig. 2.** Apilimod and Vacuolin-1 inhibit VSV-MeGFP-ZEBOV. (A) Schematic of entry assay where SVG-A cells were infected with VSV-MeGFP (MOI = 4), VSV-MeGFP-V269H (MOI = 4), or VSV-MeGFP-ZEBOV (MOI = 4). Experiments were performed in the presence of 5  $\mu$ g/mL cycloheximide (CHX) to prevent protein synthesis. Entry assay was based on the appearance of MeGFP fluorescence on the nuclear margin, on a per cell basis, of fixed infected cells visualized by fluorescence microscopy. Staining the fixed cells with Alexa647-labeled wheat germ agglutinin identified the plasma membrane of each cell (dashed outlines in C). (B) Virus infection in the absence of CHX (Left) resulted in the appearance of MeGFP fluorescence throughout the cell volume. The presence of CHX resulted in virus entry being observed by MeGFP fluorescence at the nuclear margin, which was released from incoming viral particles (Right, white arrows). (Scale bar: 10  $\mu$ m.) (C) Representative examples of maximum-Z projections images from the whole-cell volume obtained with optical sections separated by 0.3  $\mu$ m using spinning disk confocal microscopy. MeGFP fluorescence at the nuclear margin released from incoming viral particles is highlighted (white arrows). (Scale bar: 10  $\mu$ m.) (D) Quantification of the number of cells with nuclear margin labeling from three independent experiments, each determined from fields containing 59 to 90 cells (error bars show SEM). The statistical significance of the entry data was analyzed for statistical significance by one-way ANOVA and Tukey post hoc test (\*\* $P \leq 0.001$ ).

experiments, we deemed RNP delivery, as monitored by single-cell fluorescence microscopy imaging (experimental protocol summarized in Figs. 2A and 3A), to be successful when fluorescent MeGFP encapsulated in the incoming virus appeared at the nuclear margin of infected cells. The representative examples of VSV infection and RNP core release shown in Fig. 2B were obtained in the absence or presence of cycloheximide, which prevents viral protein expression. In the absence of cycloheximide (Fig. 2B, Left), large amounts of newly synthesized MeGFP are present

throughout the cell. In the presence of cycloheximide (Fig. 2B, Right), we observed MeGFP in virions (fluorescent spots) as well as released MeGFP concentrated at the nuclear margin. We scored the effect of Apilimod, Vacuolin-1, or IN1 on RNP delivery by VSV-MeGFP, VSV-MeGFP-V269H, and VSV-MeGFP-ZEBOV by determining the appearance of MeGFP at the nuclear margin in cycloheximide-treated cells. Consistent with the infection results, Apilimod, Vacuolin-1, and IN1 prevented entry of VSV-MeGFP-ZEBOV but not of VSV-MeGFP or VSV-MeGFP-V269H. As

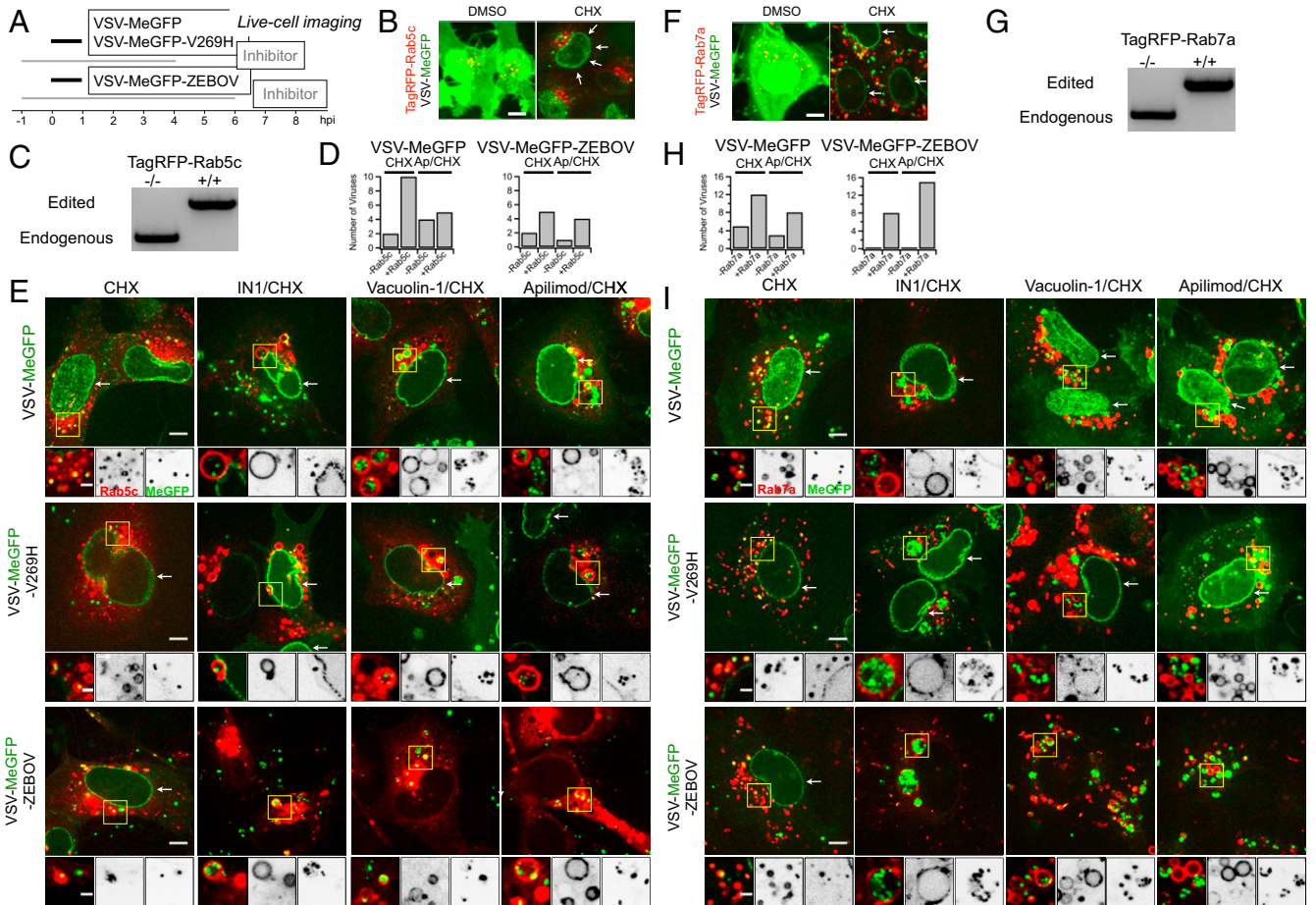


**Fig. 3.** Endolysosomal traffic of VSV-MeGFP-ZEBOV in cells expressing TagRFP-Rab5c or TagRFP-Rab7a in the presence of Apilimod or Vacuolin-1 (SI Appendix and Movies S1 and S2). (A) Schematic of live cell imaging experiment using SVG-A cells expressing fluorescently tagged TagRFP-Rab5c or TagRFP-Rab7a. Cells were infected with VSV-MeGFP, VSV-MeGFP-V269H, or VSV-MeGFP-ZEBOV (MOI = 4). Viruses trafficking (monitored with MeGFP) to the endolysosomal system (recognized by their labeling with TagRFP-Rab5c or TagRFP-Rab7a) and virus entry (established by MeGFP at the nuclear margin) were ascertained by live-cell fluorescence imaging using a spinning disk confocal microscope. (B) Visualization of VSV-MeGFP infection in TagRFP-Rab5c cells in the absence (Left) or presence (Right, white arrows) of CHX using live-cell imaging. (Scale bar: 10  $\mu$ m.) (C) Genomic PCR analysis of SVG-A cells showing biallelic integration of TagRFP into the *RAB5C* genomic locus by cotransfection of a plasmid coding for Cas9, a linear PCR product coding for the specific guide RNA targeting a region near the ATG codon of Rab5c under the control of the U6 promoter, and a template plasmid containing the RFP sequence flanked by 800 base pairs upstream and downstream of the targeted region (see Materials and Methods for more details) to generate a clonal gene-edited cell line expressing TagRFP-Rab5c. (D) Quantification of VSV-MeGFP and VSV-MeGFP-ZEBOV colocalization with Rab5c containing endosomes in the presence of CHX together with absence or presence of 5  $\mu$ M Apilimod depicted in E. Data show number of viruses that colocalized with endosomes containing or not containing Rab5c within the complete volume of the single cells depicted in E. (E) Representative examples of maximum-Z projection images from four optical sections spaced 0.35  $\mu$ m apart of virus entry without or with IN1, Vacuolin, or Apilimod for VSV-MeGFP (Top), VSV-MeGFP-V269H (Middle), and VSV-MeGFP-ZEBOV (Bottom). Each condition is in the presence of CHX. All viruses reach Rab5c-containing endosomes, but only VSV-MeGFP-ZEBOV fails to penetrate in the presence of IN1, Vacuolin-1, or Apilimod. (Scale bars: 10  $\mu$ m.) Insets correspond to a single optical section. Insets (yellow boxes) correspond to a single optical section. (Scale bars: 3  $\mu$ m.) (F) Visualization of VSV infection in TagRFP-Rab7a cells in the absence of CHX (Left) and entry in the presence of CHX (Right, white arrows). (Scale bar: 10  $\mu$ m.) (G) Genomic PCR analysis showing biallelic integration of TagRFP into the *RAB7A* genomic locus to generate a clonal gene-edited cell-line expressing TagRFP-Rab7a, using the same approach as used for *RAB5C*. (H) Quantification of VSV-MeGFP and VSV-MeGFP-ZEBOV colocalization with Rab7a containing endosomes in the presence of CHX with or without 5  $\mu$ M Apilimod within the complete cell volumes in the images depicted in I. (I) Representative examples of maximum-Z projection images from four optical sections spaced 0.35  $\mu$ m apart of virus entry without or with IN1, Vacuolin, or Apilimod for VSV-MeGFP (Top), VSV-MeGFP-V269H (Middle), and VSV-MeGFP-ZEBOV (Bottom). All viruses reach Rab7a-containing endosomes, but only VSV-MeGFP-ZEBOV fails to penetrate in the presence of IN1, Vacuolin-1, or Apilimod. (Scale bars: 10  $\mu$ m.) Insets correspond to a single optical section. Insets (yellow boxes) correspond to a single optical section. (Scale bars: 3  $\mu$ m.)

expected, Bafilomycin A1 blocked entry of all viruses (images in Fig. 2C and quantification in Fig. 2D).

**Intracellular Trafficking of Virus Particles in the Presence of Apilimod or Vacuolin-1.** Internalized virus particles traffic along the endocytic pathway to reach the endosomal compartment(s) from which membrane fusion and genome entry into the cytosol occur. To establish the identity of the endosomal compartments, we

used genome editing in SVG-A cells (Figs. 3 C and G and 4 B and D) to replace expression of a subset of proteins enriched in different endosomal compartments (the small GTPases Rab5c and Rab7a, EEA1, or NPC1) with their corresponding fluorescent chimeras obtained by fusion with TagRFP, mScarlet, or Halo (Figs. 3 B, E, F, and I and 4 C and E). The lack of fluorescently tagged filipin (a cholesterol binder) in the endolysosomal compartment in the absence but not in the presence of

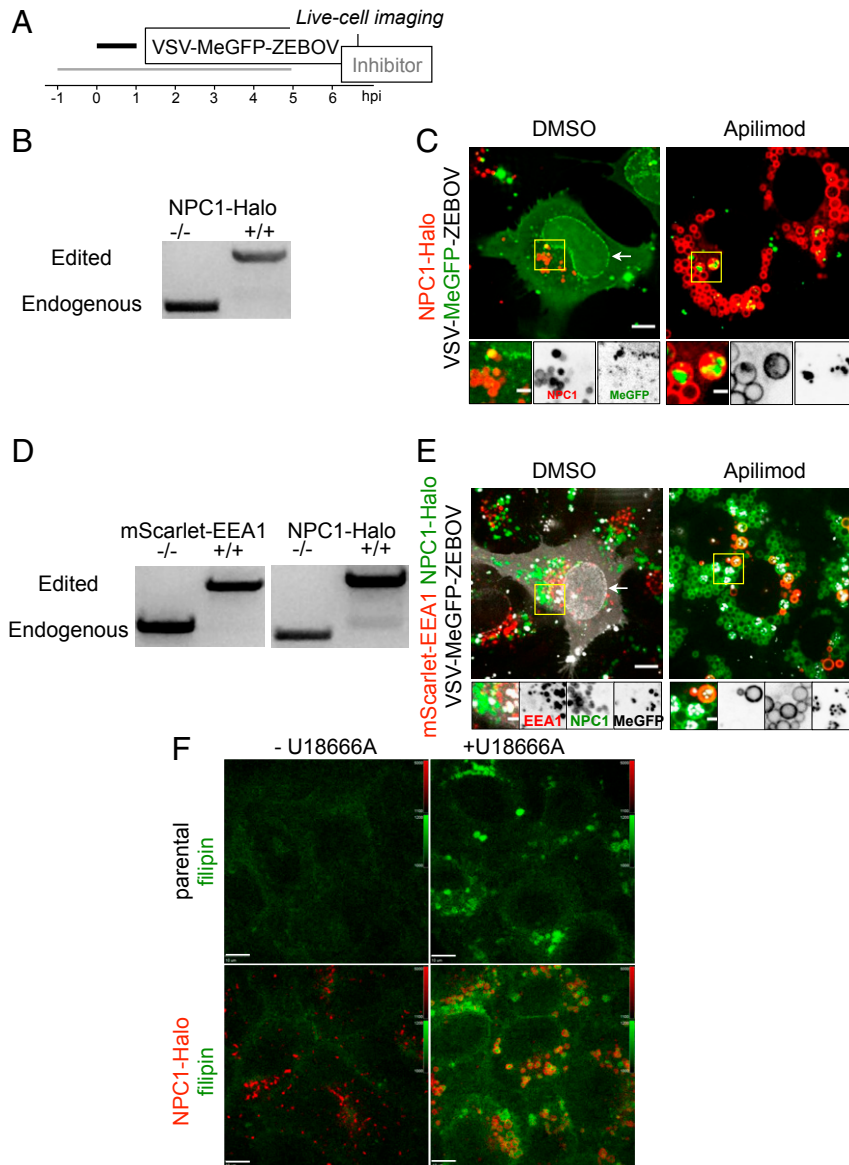


**Fig. 4.** Endolysosomal traffic of VSV-MeGFP-ZEBOV in cells expressing NPC1-Halo or coexpressing mScarlet-EEA1 and NPC1-Halo in the presence of Apilimod (*SI Appendix* and *Movie S3*). (A) Schematic of live-cell imaging experiment with gene-edited SVG-A cells expressing NPC1-Halo or NPC1-Halo together with mScarlet-EEA1. Halo was labeled with either JF549 or JF647. Cells were infected with VSV-MeGFP-ZEBOV (MOI = 3). (B) Genomic PCR analysis showing biallelic integration of Halo into the *NPC1* genomic locus to generate a clonal gene-edited cell line expressing NPC1-Halo, using the same approach as for *RAB5C* and *RAB7A*. (C) Representative examples of maximum-Z projection images from four optical sections spaced 0.25  $\mu\text{m}$  apart in the absence (*Left*) and presence (*Right*) of Apilimod, showing that VSV-MeGFP-ZEBOV reached NPC1-Halo–containing endosomes even in the presence of Apilimod, while failing to penetrate and infect. (Scale bar: 10  $\mu\text{m}$ .) *Insets* correspond to a single optical section. (Scale bar: 3  $\mu\text{m}$ .) (D) SVG-A cells with genomic NPC1-Halo were further gene edited to contain EEA1 tagged with mScarlet. Genomic PCR analysis shows biallelic integration into the *EEA1* locus of mScarlet-EEA1 (*Left*) and into the *NPC1* locus of NPC1-Halo (*Right*). (E) Representative examples of maximum-Z projection images in the absence (*Left*) and presence (*Right*) of Apilimod, showing that VSV-MeGFP-ZEBOV reached endosomes containing mScarlet-EEA1 and endosomes containing both mScarlet-EEA1 and NPC1-Halo in the presence of Apilimod, while failing to penetrate and infect. (Scale bar: 10  $\mu\text{m}$ .) *Insets* correspond to a single optical section. (Scale bar: 3  $\mu\text{m}$ .) (F) Representative images of parental cells (*Top*) and gene-edited SVG-A cells expressing NPC1-Halo (*Bottom*) incubated with filipin III (naturally fluorescent polyene antibiotic that binds to cholesterol) in the absence (*Left*) and presence (*Right*, NPC1 inhibitor of cholesterol export) of U18666A, showing NPC1-Halo is a functional cholesterol transporter. (Scale bar: 10  $\mu\text{m}$ .)

U18666A, a potent inhibitor of NPC1 (Fig. 4F), showed that NPC1-Halo remained active as a cholesterol transporter.

Using live-cell spinning disk confocal microscopy (Figs. 3 and 4), we monitored the presence of virus particles in the fluorescently tagged endosomes by colocalization with the fluorescent spots from the virus-incorporated MeGFP. We monitored entry by carrying out the experiments in the presence of cycloheximide, thus ensuring that any MeGFP fluorescent signal at the nuclear margin originated only from MeGFP molecules carried by incoming viral particles (Fig. 3 B and F). All cells were maintained at 37 °C throughout all phases of the experiment to ensure normal and undisturbed intracellular trafficking. All control experiments performed in the absence of inhibitors showed arrival of VSV-MeGFP, VSV-MeGFP-V269H, or VSV-MeGFP-ZEBOV virus particles to early (Rab5c and EEA1) (Figs. 3E and 4E) or late (Rab7a or NPC1) endosomes and lysosomes (Figs. 3I and 4 C and E). MeGFP released from all viruses appeared at the nuclear margin, showing effective RNP release. NPC1, the receptor for VSV-MeGFP-ZEBOV entry, is required for fusion from endosomes (2). The successful VSV-MeGFP-ZEBOV infection observed in the absence of drug in cells expressing NPC1-

Halo alone or in combination with mScarlet-EEA1 indicates that NPC1-Halo is capable of facilitating infection and that VSV-MeGFP-ZEBOV trafficked to NPC1-Halo-containing endosomes.

Apilimod and Vacuolin-1 treatment of the SVG-A cells led to enlargement and vacuolization of their endosomes and lysosomes tagged with fluorescent EEA1, Rab5c, Rab7a, or NPC1 (Figs. 3–5), in agreement with earlier PIKfyve ablation studies (13, 21). VSV-MeGFP and VSV-MeGFP-V269H (fluorescent dots, white) reached all tagged species of enlarged endolysosomes and successfully penetrated into the cytosol, as indicated by MeGFP at the nuclear margin (Fig. 3 E and I). VSV-MeGFP-ZEBOV also trafficked to all tagged species of enlarged endolysosomes (Fig. 3 E and I), often reaching one of the numerous NPC1-containing vacuoles enriched in EEA1 (Figs. 4E and 5 B and C). VSV-MeGFP-ZEBOV in EEA1-containing endosomes increased in the presence of Apilimod, as also reported for VLP ZEBOV (27). While able to reach NPC1-containing functional endosomes in cells treated with Apilimod (Figs. 4 C and E and 5 B and C), VSV-MeGFP-ZEBOV failed to penetrate into the cytoplasm, as reflected by absence of MeGFP in the nuclear margin (Figs. 2C, 3 E and I, 4 C and E, and 5B).

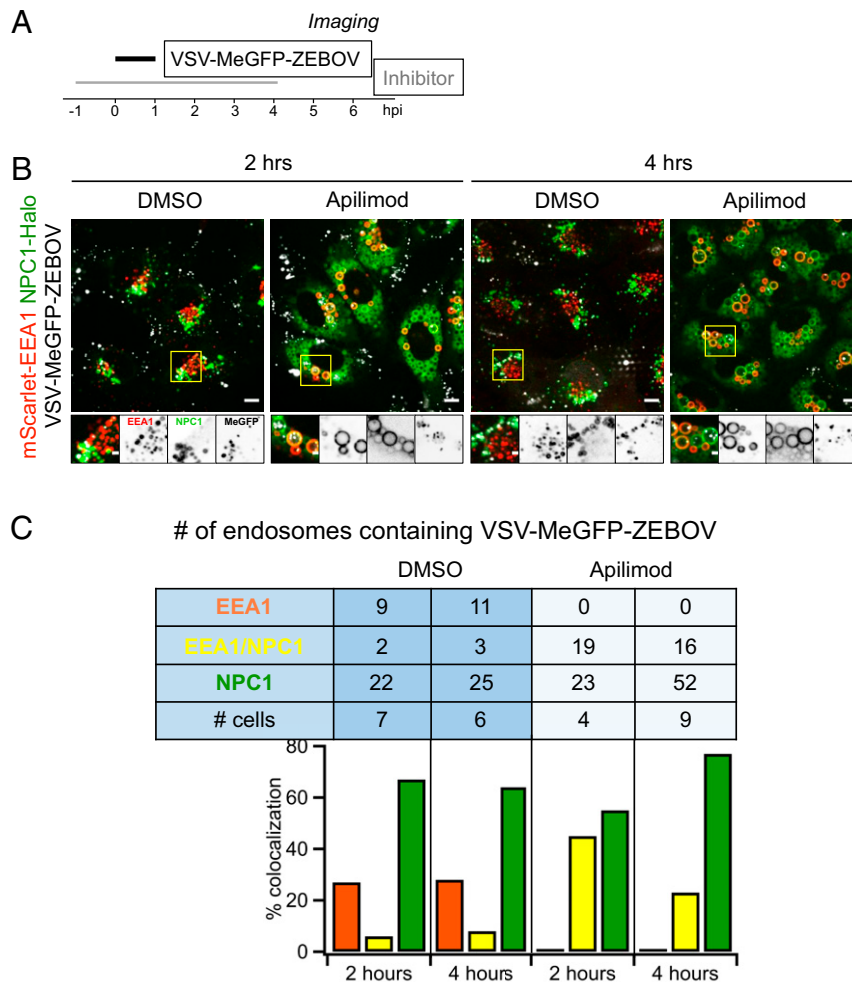


**Fig. 5.** Extent of VSV-MeGFP-ZEBOV traffic into endosomes enriched in NPC1-Halo or NPC1-Halo and mScarlet-EEA1. (A) Schematic of imaging experiment of VSV-MeGFP-ZEBOV trafficking in NPC1-Halo or NPC1-Halo and mScarlet-EEA1 gene-edited SVG-A cells. (B) Representative examples of maximum-Z projection images from four optical sections spaced 0.25  $\mu\text{m}$  apart in the absence and presence of Apilimod 2 h or 4 h postinfection. A large number of VSV-MeGFP-ZEBOV but not of VSV-MeGFP particles accumulated in the endosomes enlarged upon Apilimod treatment. (Scale bar: 10  $\mu\text{m}$ .) (C) Quantification of VSV-MeGFP-ZEBOV colocalization with mScarlet-EEA1 alone, both mScarlet-EEA1 and NPC1-Halo, or NPC1-Halo alone 2 h and 4 h postinfection, in the absence or presence of 5  $\mu\text{M}$  Apilimod. Data obtained from complete cell volumes are presented as numbers and corresponding percent colocalizations of VSV-MeGFP-ZEBOV particles associated with a given type of endosome.

**Apilimod Blocks Infection of VSV SARS-CoV-2.** Using a recombinant VSV expressing soluble eGFP (VSV-eGFP) where the glycoprotein (GP) was replaced with that of ZEBOV GP (VSV-eGFP-ZEBOV) or SARS-CoV-2 S (VSV-eGFP-SARS-CoV2), we inoculated MA104 cells with these chimera viruses and tested the effects of Apilimod on infection by flow cytometry (Fig. 6A). We found potent inhibition of VSV-eGFP-SARS-CoV-2 infection by Apilimod and confirmed that the compound also inhibits VSV-eGFP-ZEBOV infection (Fig. 6B). The dose-response curves indicated similar effects for VSV-eGFP-ZEBOV and VSV-eGFP-SARS-CoV-2 ( $IC_{50}$ s of  $\sim 50$  nM), in contrast to the absence of any detectable inhibition of VSV-eGFP infection, used here as a negative control.

**Apilimod Blocks Infection of SARS-CoV-2 Virus.** To test the effect of Apilimod on bona fide SARS-CoV-2 infection, we exposed Vero E6 cells to fully infectious SARS-CoV-2 (strain 2019-nCoV/USA-WA1/2020); after 24-h incubation, supernatants were harvested and titered by focus-forming assay on a separate set of Vero E6 cells (Fig. 7A). Apilimod strongly inhibited SARS-CoV-2 infection, and the dose-response curve was similar or more potent than those observed for VSV-eGFP-ZEBOV or VSV-eGFP-SARS-CoV-2 ( $IC_{50}$ s of  $\sim 10$  nM) (Fig. 7B).

## Discussion

Coronaviruses, filoviruses, and arenaviruses have different replication strategies and unrelated surface GPs that engage different receptor molecules during entry (1, 2, 5–8). Coronavirus

and filovirus surface GPs share a requirement for entry-associated proteolytic processing for activation as fusogens (1). Filoviruses require passage through low-pH compartments where cathepsins are active. Coronaviruses may enter directly by fusion at the plasma membrane or following receptor-mediated endocytosis. Cell entry of SARS-CoV and SARS-CoV-2 depends on the protease TMPRSS2 in conjunction with ACE2 (34–37), and, when TMPRSS2 is present, the entry pathway becomes insensitive to cathepsin inhibition (34, 37, 38).

The common inhibition of viruses from all three groups by Apilimod is a consequence of perturbing their shared entry pathway. Moreover, it is not the cathepsin activity itself that these compounds affect, judging from the outcome of the assays with Apilimod and Vacuolin-1 showing they inhibit VSV chimeras bearing the surface GPs of ZEBOV and LCMV and, to a lesser extent, LASV. Apilimod also inhibits infection of cells by VSV-SARS-CoV-2 as well as by authentic SARS-CoV-2; neither compound blocks infection by wild-type VSV. For VSV-ZEBOV, we have shown that the virus reaches a compartment enriched in NPC1, the ZEBOV coreceptor, and often also enriched in EEA1, but that it nonetheless fails to release internal proteins into the cytosol. Apilimod does not inhibit cathepsin (26), but Apilimod (39) and Vacuolin-1 (17, 23) can interfere with cathepsin maturation, as evidenced by an increase in procathepsin in treated cells; they do not influence endosomal pH (18, 26, 40), although other studies report that Apilimod decreases cathepsin activity (41) and Vacuolin-1 increases pH (17, 23). Irrespective of this discrepancy, both Apilimod and Vacuolin-1 inhibit PIKfyve (17, 19), a

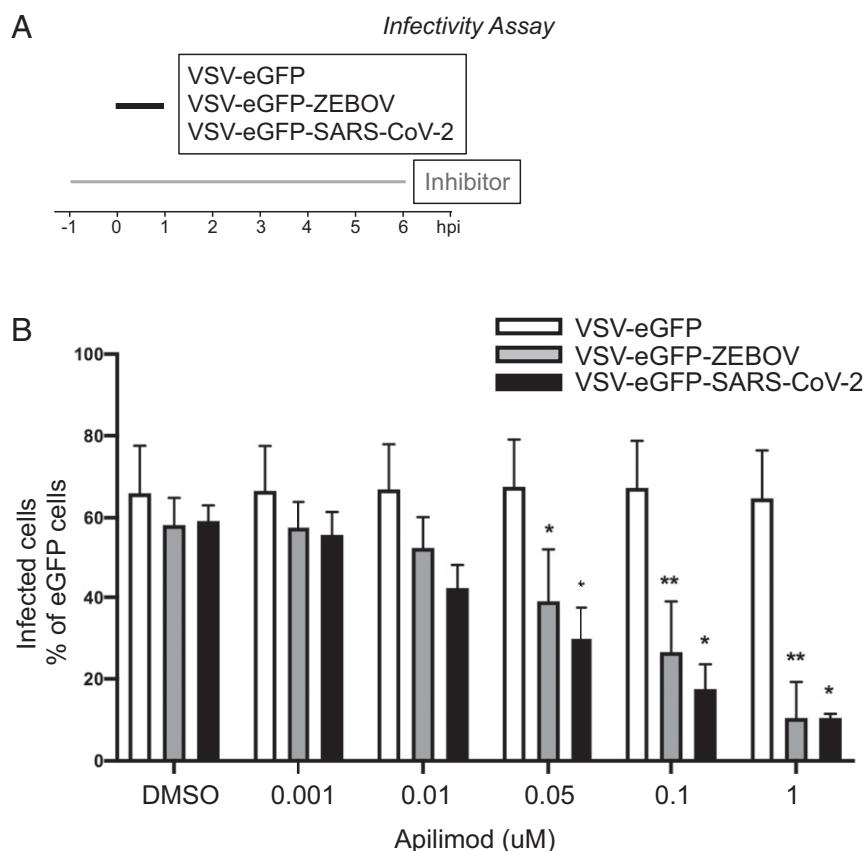


**Fig. 6.** Apilimod and Vacuolin-1 inhibit infection of VSV-eGFP-SARS-CoV-2. (A) Schematic of infectivity assay of VSV-eGFP, VSV-eGFP-ZEBOV, and VSV-eGFP-SARS-CoV-2 in MA104 cells. MA104 cells were pretreated for 1 h with the indicated concentration of Apilimod. Pretreated cells were inoculated with the indicated virus (MOI = 1) for 1 h at 37 °C. At 6 h postinfection cells were harvested, and the fraction of cell expressing eGFP cells was quantified by flow cytometry. (B) Quantification of the infectivity is shown with averages  $\pm$  SEM from three independent experiments. Statistical significance was determined using a *t* test (\* $P \leq 0.05$ ; \*\* $P \leq 0.01$ ).

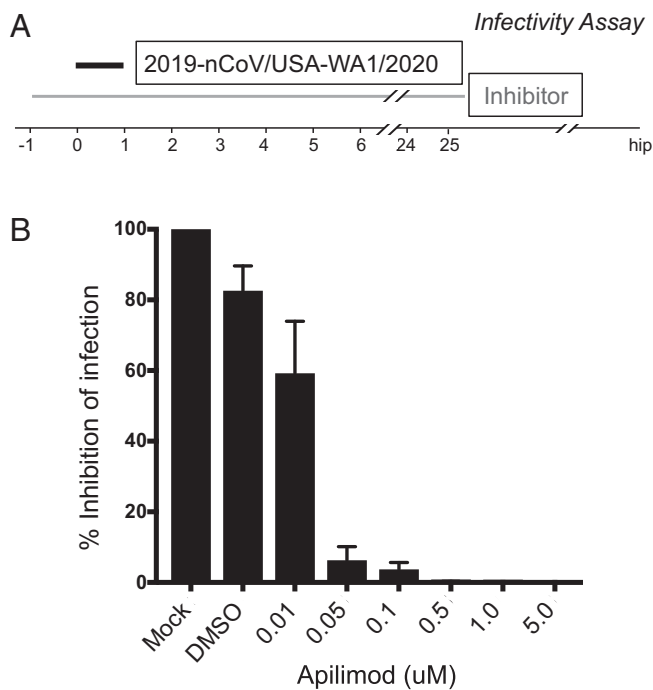


**Fig. 7.** Apilimod inhibits infection of SARS-CoV-2 virus. (A) Schematic of infectivity assay of fully infectious Sars-CoV-2 (strain 2019-nCoV/USA-WA1/2020). Vero E6 cell monolayers were pretreated with medium containing DMSO or serial dilutions of Apilimod at the indicated concentrations. SARS-CoV-2 was diluted (MOI = 0.01) in Apilimod-containing medium and added to Vero E6 cells for 1 h at 37 °C. After adsorption, the viral inocula were removed, and medium containing the respective concentration of Apilimod was reapplied. After 24-h incubation, supernatants were harvested and titrated by focus-forming assay on a separate set of Vero E6 cells. (B) Quantification of the infectivity is shown with averages  $\pm$  SEM from three independent experiments per condition and expressed as the percent infection relative to mock-treated SARS-CoV-2 infected cells.

three-subunit complex (14) with a PI-3P-binding FYVE domain (10, 11) that recognizes the endosomal marker, PI-3-P. Functional ablation of this enzyme by genetic means (12, 15) gives rise to the same cellular phenotype as treatment with either compound (17–19). The similar dose–response curves for Apilimod inhibition of the ZEBOV and SARS-CoV-2 chimeras ( $IC_{50}$  of  $\sim 50$  nM) and of authentic SARS-CoV-2 virus ( $IC_{50}$  of  $\sim 10$  nM) are in good agreement with the  $IC_{50}$  of  $\sim 15$  nM for Apilimod inhibition of PIKfyve in vitro (19). Thus, perturbing normal endosomal trafficking by inhibiting PIKfyve activity suggests it is the mechanism by which Apilimod and Vacuolin-1 block entry of such a diverse set of viral pathogens.

One of the most striking consequence of PIKfyve inhibition, and hence of PI-3,5-P<sub>2</sub> restriction in endosomal membranes, is the swelling of endosomes into small, spherical vacuoles—the phenomenon that gave Vacuolin-1 its name (18). Our imaging data with VSV-MeGFP-ZEBOV chimeras show that the virus particles accumulating in these structures, many of which also contain the NPC1 coreceptor (2, 42), often appear to be relatively immobile and adjacent to the endosomal limiting membrane. One possible explanation is that, when a virion reaches these distended endosomes, it can bind or remain bound to the limiting membrane, but not fuse. Another is that virions may fuse with smaller intraluminal vesicles in the endosomal lumen (43), but that PI-3,5-P<sub>2</sub> depletion prevents back-fusion of these vesicles with the endosomal limiting membrane and inhibits release into the cytosol of the viral genome.

Inhibition of infection by authentic SARS-CoV-2 shows that the blocked release of the viral genome from a vacuolated endosome is independent of the shape, size, and distribution of spike protein on the virion. The assay we used to determine effects on infectivity of authentic virus measured release of virions after multiple rounds of infection, rather than entry, which we monitored in the VSV-SARS-CoV-2 experiments by detecting eGFP synthesis in the cytosol. Nevertheless, the  $IC_{50}$  of Apilimod in experiments with authentic virus is remarkably similar to (or even more potent than) that obtained with chimeric VSV-SARS-CoV-2.

Although cathepsin L inhibitors block SARS-CoV and SARS-CoV-2 infection in cell culture (4, 5), they have less pronounced effects when tested in animals (44). This may be because another protease, TMPRSS2 on the surface of cells in relevant tissues, appears to prime SARS-CoV (44) and SARS-CoV-2 (37) spike proteins for efficient entry. As the effectiveness of Apilimod and Vacuolin-1 does not depend on cathepsin inhibition, their capacity to block entry of several distinct families of viruses is likely to be independent and downstream of the protease that primes their surface GP for fusion. Phase I and phase II clinical trials have shown that Apilimod is safe and well tolerated (24, 25, 29, 30). The trials were discontinued because of lack of effectiveness against the autoimmune condition for which the drug was tested. We suggest that one of these compounds, or a potential derivative, could be a candidate broad-spectrum therapeutic for several emerging human viral pathogens, including SARS-CoV-2.

## Material and Methods

**Cell Culture.** Human astroglial SVG-A derived cells (a kind gift from Walter J. Atwood, Brown University, Providence, RI) were grown at 37 °C and 5% CO<sub>2</sub> in Minimum Essential Medium (MEM) (10-010-CV; Corning) supplemented with 10% heat-inactivated fetal bovine serum (FBS, S11150; Atlanta Biologicals), penicillin, and streptomycin (1406-05-9; VWR International). African Green Monkey kidney epithelial MA104 cells (a kind gift from Siyuan Ding, Washington University in St. Louis, St. Louis, MO) were grown at 37 °C and 5% CO<sub>2</sub> in Medium 199 supplemented with 10% heat-inactivated FBS. Vero C1008 (Vero 76, clone E6, Vero E6) [American Type Culture Collection (ATCC) CRL-1586] cells were cultured in Dulbecco's Modified Eagle Medium (DMEM) supplemented with 10% FBS, and penicillin and streptomycin. Vero CCL-81 (ATCC CCL-81) cells were maintained in DMEM supplemented with 10% FBS, 10 mM HEPES pH 7.4, 1% Glutamax, and penicillin/streptomycin.

**Reagents.** Vacuolin-1 (18) was custom synthesized; Apilimod (HY-14644) was from MedChem Express, IN1 was a kind gift from N. Gray, Dana-Farber Cancer Institute and Harvard Medical School, Boston, MA (33), U-18666A (10009085) and Filipin III (70440) were from Cayman Chemical, Bafilomycin A1 (B1793-2UG) was from Sigma-Aldrich, Cycloheximide (239764) was from Calbiochem, and wheat germ agglutinin conjugated with Alexa Fluor-647 (W32466) was from ThermoFisher.

**Viruses.** Recombinant VSV (Indiana serotype) expressing MeGFP alone which initiates fusion at pH < 6.2 (VSV-MeGFP) (45) (or in combination with V269H GP, VSV-MeGFP-V269H), RABV GP (VSV-MeGFP-RABV) (46), LASV GP (VSV-MeGFP-LASV) (7), LCMV GP (VSV-MeGFP-LCMV), Zaire EBOV GP (VSV-MeGFP-ZEBOV) (47), or SARS-CoV-2 S Wuhan-Hu-1 strain (VSV-eGFP-SARS-CoV-2—description to be published elsewhere) were used for infection, entry, and live-cell imaging assays. All viruses were generated and recovered according to ref. 48.

SARS-CoV-2 strain 2019-nCoV/USA-WA1/2020 was obtained from the Centers for Disease Control and Prevention (gift of Natalie Thornburg, Centers for Disease Control, Atlanta, GA). Virus was passaged once in Vero CCL81 cells (ATCC) and titrated by focus-forming assay also on Vero E6 cells.

**Genome Editing.** Individual cell lines of SVG-A were gene edited in both alleles using the CRISPR-Cas9 system to incorporate fluorescent tags into the N terminus of Rab5c (TagRFP), Rab7a (TagRFP), EEA1 (mScarlet), or the C terminus of NPC1 (Halo). The NPC1-Halo expressing cells were further gene edited to incorporate mScarlet-EEA1 creating SVG-A cells simultaneously expressing mScarlet-EEA1 and NPC1-Halo.

A free PCR strategy (49, 50) was used to generate small guide RNAs (sgRNA) with target sequences for either Rab5c, Rab7a, NPC1, or EEA1 (Table 1).

**Table 1. Primer sequences used to generate the sgRNAs and corresponding genomic fragments**

Primer	Orientation	Nucleotide sequence
U6 promoter	F	GCCGGTACCTGAGGGCCTATTTCCC
	R	ACCTCTAGAAAAAAGCACCGACTCGGTGCCACTTTTTCAAGTTGATA ACGGACTAGCCTTATTTAACTTGCTATTTCTAGCTCTAAAACNNNNN NNNNNNNNNNNNNNCGGTGTTTCGCTTCCACAAG
Target sequence Rab5c	R	GACCCGCCATTGCCGTCCA
Target sequence Rab7a	R	TCAAATAAAGGGGAAAAG
Target sequence NPC1	R	TAAATTTCTAGCCCTCTCGC
Target sequence EEA1	R	GGTGGTGGTTAAACCATG
Primers Rab5c	F1up	gaattcgagctcgttaccGAGAGAAGGATCAG
	R1up	TGCCCGTCCAGCTGTAGTG
	F2 RFP	CCACTACAGCTGGACGGGCAatggtgtctaaggcgaagagc
	R2 RFP	GGAACCACCAGAACCACCAGAA
	F3 down	GGTCTGGTGGTTCTGGTGGTTCCCTGGCGGTCGGGGAGGCGCA
Primers Rab7a	R3 down	gtcgactctagagatccccCTCCTACCAAGAGAGTAGAGAAAAG
	F1up	gaattcgagctcgttaccACTGCTGTGAGCCTTGCCTTCA
	R1up	CCTTCAAATAAAGGGGAAAAGG
	F2 RFP	CCTTTTCCCCTTTAGTTGAAGGatggtgtctaaggcgaag
	R2 RFP	GGAACCACCAGAACCACCAGAA
Primers NPC1	F3 down	TTCTGGTGGTTCTGTGGTTCACCTCTAGGAAGAAAAGTGTGCTG
	R3 down	gtcgactctagagatccccCTCACCAACCTACCAGAAAT
	F1up	gaattcgagctcgttaccCCACTGAGATGAAGGAGTCCAT
	R1up	GAAATTTAGAAGCCGTTGCGCG
	F2 Halo	CGCGAACGGCTTCTAAATTTcggaggttctggtgttctggtgttccGCAGAA ATCGGTAAGCTTCCCA
Primers EEA1	R2 Halo	GCCGGAAATCTCGAGCGTCGACAG
	F3 down	CTGTCGACGCTCGAGATTTCCGGCtagccctctcagggcatcc
	R3 down	gtcgactctagagatccccGCTGTCTAATGAACTTCTAGGTC
	F1 up	gaattcgagctcgttaccCTTTGGCTGAAATTAGAAGCAGG
	R1 up	CATGGTTTAACCAACCCCGCG
Primers EEA1	F2 mScarlet	CGCCGGTGGTGGTTAAACCATGtgtagcaaggggcagggcagtgat
	R2 mScarlet	cttgtagactcgtccatccgc
	F3 down	GCGGCATGGACGAGCTGTACAAGggaggttctggtgttctggtgttccTTAA GGAGGATTTACAGAGGGTAAGAG
	R3 down	gtcgactctagagatccccGCTCTAATCTTTCTATCCTCAAGGTTTTT

The sgRNAs with target sequences specific for Rab5c, Rab7a, NPC1, or EEA1 were generated using a free PCR strategy using a U6 promoter-containing primer and reverse primers including Rab5c, Rab7a, NPC1, or EEA1 specific target nucleotide sequences (at the positions indicated with N).

The genomic DNA fragment of Rab5c, Rab7a, NPC1, or EEA1 genes fused with either TagRFP, Halo, or mScarlet were cloned into the pUC19 vector (donor constructs) which then served as homologous recombination repair templates for the Cas9 enzyme-cleaved genomic DNA. Donor constructs were obtained by a ligation of PCR amplification products from the genomic DNA fragments, TagRFP, Halo, and mScarlet sequences. Primers F1-R1 and F3-R3 amplified ~800 base pairs of genomic sequences upstream and downstream of the start codon of Rab5c, Rab7a, or EEA1 or the stop codon of NPC1, respectively (Table 1). Primers F1 and R3 contain sequences complementary to the pUC19 vector linearized using the SmaI restriction enzyme (lowercase in the primer sequences). The TagRFP sequence containing the GGS peptide linker was amplified using primers F2-R2 from a TagRFP mammalian expression plasmid used as a template. The F2 primer contains complementary sequences to the 3' end of the F1-R1 fragment, while the F3 primer contains complementary sequences to the 3' end of the TagRFP sequences.

PCR products (fragments F1-R1, F2-R2, and F3-R3) were subjected to electrophoresis in 1% agarose and gel purified using a purification kit from Zymogen. The PCR fragments were cloned into the linearized pUC19 vector using the Gibson Assembly Cloning Kit (E55105; New England Biolabs).

SVG-A cells ( $1.5 \times 10^5$  cells) were cotransfected with 0.8  $\mu$ g of *Streptococcus pyogenes* Cas9, 0.8  $\mu$ g of free PCR product coding for the target sgRNA, and 0.8  $\mu$ g of pUC19 vector using Lipofectamine 2000 reagent (Invitrogen) according to the manufacturer's instructions. Transfected cells were grown for 7 d to 10 d and sorted for TagRFP, Halo, or mScarlet expression using fluorescence-activated cell sorting (FACS) (SH-8005; Sony). Prior to FACS, NPC1-Halo cells were labeled for 15 min with Janelia Fluor 647 (JF647). Single cells expressing the desired chimera were isolated, clonally expanded, and then screened by genomic PCR for TagRFP, Halo, or mScarlet insertion into both alleles (primers listed in Table 2).

**Infection Assays.** SVG-A cells were plated at about 30 to 40% confluency into 24-well plates and incubated for 1 d at 37 °C and 5% CO<sub>2</sub>. At the start of the experiment, cells were incubated with the indicated drug or dimethyl sulfoxide (DMSO) at 37 °C for 1 h. Following this, cells were incubated for 1 h at 37 °C with VSV, VSV-MeGFP-V269H, VSV-MeGFP-RABV, VSV-MeGFP-LASV, VSV-MeGFP-LCMV, or VSV-MeGFP-ZEBOV in drug- or DMSO-containing infection medium ( $\alpha$ -MEM, 50 mM Hepes, 2% FBS). Cells were then washed to remove nonadsorbed viruses and further incubated at 37 °C in medium containing the drug or DMSO, with experiments ending at the indicated times by fixation with 3.7% formaldehyde in phosphate-buffered saline (PBS). Fluorescent intensity from 20,000 single cells from a single round of

**Table 2. Primer sequences used for screening**

Primer	Orientation	Nucleotide sequence
Rab5c	F	GAGCCTGAAGTTGGGAGACC
Rab5c	R	CATGCCACTCACCTCCAAT
Rab7a	F	GCGGTCACTCTTTGAGAAAAGT
Rab7a	R	AAGTGGCAGCACGGACAGTGT
NPC1	F	TCTCAAAAAGAGAGGGAGAGAGAT
NPC1	R	AAGTTTAGTGTCTGTGTTGCCT
EEA1	F	CATCTGTCAAGTACGGGGGCTG
EEA1	R	CGGCACCACACCTCCAGCTC

Primers used for PCR amplification and subsequent DNA sequencing to verify presence of genome-edited double alleles.

infection was determined by flow cytometry using a BD FACSCanto II equipped with DIVA software package.

MA104 cells were pretreated for 1 h with the indicated concentration of Apilimod or DMSO. Pretreated cells were inoculated with VSV-eGFP, VSV-eGFP-ZEBOV, or VSV-eGFP-SARS-CoV-2 at a multiplicity of infection (MOI) = 1 (based on titers in MA104 cells) in the presence of Apilimod or DMSO for 1 h at 37 °C. At 6 to 8 h postinfection, cells were collected and fixed in 2% paraformaldehyde (PFA) and then subjected to flow cytometry. The percentage of GFP cells was determined using FlowJo software (Tree Star Industries).

Vero E6 cell monolayers were pretreated for 1 h at 37 °C with serial dilutions of Apilimod at the indicated concentrations. Next, SARS-CoV-2 was diluted to an MOI of 0.01 focus-forming units per cell in Apilimod-containing medium and added to Vero E6 cells for 1 h at 37 °C. After adsorption, cells were washed once with PBS, and medium containing the respective concentration of Apilimod was added. Cells were incubated for 24 h at 37 °C, at which time cell culture supernatants were removed and used for determination of viral titer by focus forming assay.

**SARS-CoV-2 Focus-Forming Assay.** Cell culture supernatants from virus-infected cells were diluted serially 10-fold, added to Vero E6 cell monolayers in 96-well plates, and incubated at 37 °C for 1 h. Subsequently, cells were overlaid with 1% (wt/vol) methylcellulose in MEM supplemented with 2% FBS. Plates were harvested 30 h later by removing overlays and fixed with 4% paraformaldehyde in PBS for 20 min at room temperature. Plates were washed and sequentially incubated with 1 µg/mL CR3022 anti-spike antibody (51) and HRP-conjugated goat anti-human IgG in PBS supplemented with 0.1% saponin and 0.1% bovine serum albumin (BSA). SARS-CoV-2-infected cell foci were visualized using TrueBlue peroxidase substrate (KPL) and quantitated on an ImmunoSpot microanalyzer (Cellular Technologies). Data were processed using Prism software (GraphPad Prism 8.0), and viral titers are reported as percent inhibition relative to mock-treated SARS-CoV-2-infected cells.

**Entry Assay and Intracellular Traffic.** SVG-A cells plated on glass #1.5 coverslips at about 30 to 40% confluency 1 d prior to experiment were treated with drug or DMSO for 1 h at 37 °C. Following this, cells were incubated at 37 °C with VSV, VSV-MeGFP-V269H, VSV-MeGFP-RABV, VSV-MeGFP-LASV, VSV-MeGFP-LCMV, or VSV-MeGFP-ZEBOV in drug- or DMSO-containing infection medium. After this, cells were washed, then further incubated in medium containing the drug or DMSO at 37 °C, with the experiment ending at

the indicated time by fixation for 20 min at room temperature with 3.7% formaldehyde in PBS. This was followed with a 10-min incubation of 5 µg/mL Alexa647-labeled wheat germ agglutinin in PBS to label the outline of the cells.

Cells were imaged using a spinning disk confocal microscope with optical planes spaced 0.3 µm apart (52). The entry assay scored the presence of MeGFP at the nuclear margin in each cell. Trafficking of viruses to endosomal compartments was observed using live-cell imaging using the spinning disk confocal microscope. Chemical fixation tends to eliminate the large endolysosomal vacuoles generated by Vacuolin-1 or Apilimod and reduces the colocalization with viral particles contained within. Time series with images taken every 3 s for 3 min in a single optical plane with the appropriate fluorescent channels (52) were acquired from nonfixed samples imaged at the end of the experimental period. For experiments containing NPC1-Halo, the Halo-tagged cells were labeled with either 250 nM JF549 or JF647 dye in media for 30 min at 37 °C. Following labeling, cells were washed three times with media. The microscope was operated using the Slidebook 6.4 software package (31), and images were displayed also using this software.

**Statistical Tests.** To compare the means from cells with different treatments, one-way ANOVA and post hoc Tukey test analysis were used to take into account unequal sample sizes as indicated in the Figs. 1, 2, and 6 figure legends.

**Data Availability.** The VSV virus chimeras are available from the corresponding author S.P.W. upon request.

All study data are included in the article and *SI Appendix* and *Movies S1–S3*.

**ACKNOWLEDGMENTS.** We thank Walter J. Atwood for providing the parental SVG-A cells; Eric Marino, Justin H. Houser, and Tegy John Vadakkan for maintaining the spinning disc confocal microscope (T.K. Laboratory); Marina Cella and Erica Lantelme from the flow cytometry facility, Department of Pathology and Immunology at WUSM for help with flow cytometry; Stephen C. Harrison for helpful discussions and editorial assistance; and Alex J. B. Kreuztberger for editorial help. This research was supported by NIH funding (Grant AI109740) to S.P.J.W. and T.K., by NIH Maximizing Investigators' Research Award (MIRA) GM130386 to T.K., by NIH funding (AI059371) and unrestricted funds from WUSM to S.P.J.W., and by NIH Contract 75N93019C00062 and NIH Grant R01 AI127828 to M.S.D.

1. K. Chandran, N. J. Sullivan, U. Felber, S. P. Whelan, J. M. Cunningham, Endosomal proteolysis of the Ebola virus glycoprotein is necessary for infection. *Science* **308**, 1643–1645 (2005).
2. J. E. Carette *et al.*, Ebola virus entry requires the cholesterol transporter Niemann-Pick C1. *Nature* **477**, 340–343 (2011).
3. I.-C. Huang *et al.*, SARS coronavirus, but not human coronavirus NL63, utilizes cathepsin L to infect ACE2-expressing cells. *J. Biol. Chem.* **281**, 3198–3203 (2006).
4. G. Simmons *et al.*, Inhibitors of cathepsin L prevent severe acute respiratory syndrome coronavirus entry. *Proc. Natl. Acad. Sci. U.S.A.* **102**, 11876–11881 (2005).
5. X. Ou *et al.*, Characterization of spike glycoprotein of SARS-CoV-2 on virus entry and its immune cross-reactivity with SARS-CoV. *Nat. Commun.* **11**, 1620 (2020).
6. W. Cao *et al.*, Identification of alpha-dystroglycan as a receptor for lymphocytic choriomeningitis virus and Lassa fever virus. *Science* **282**, 2079–2081 (1998).
7. L. T. Jae *et al.*, Virus entry. Lassa virus entry requires a trigger-induced receptor switch. *Science* **344**, 1506–1510 (2014).
8. G. Pasqual, J. M. Rojek, M. Masin, J.-Y. Chatton, S. Kunz, Old world arenaviruses enter the host cell via the multivesicular body and depend on the endosomal sorting complex required for transport. *PLoS Pathog.* **7**, e1002232 (2011).
9. J. G. Carlton, P. J. Cullen, Coincidence detection in phosphoinositide signaling. *Trends Cell Biol.* **15**, 540–547 (2005).
10. D. Sbrissa, O. C. Ikonomov, A. Shisheva, PIKfyve, a mammalian ortholog of yeast Fab1p lipid kinase, synthesizes 5-phosphoinositides. Effect of insulin. *J. Biol. Chem.* **274**, 21589–21597 (1999).
11. A. Shisheva, D. Sbrissa, O. Ikonomov, Cloning, characterization, and expression of a novel Zn<sup>2+</sup>-binding FYVE finger-containing phosphoinositide kinase in insulin-sensitive cells. *Mol. Cell. Biol.* **19**, 623–634 (1999).
12. O. C. Ikonomov, D. Sbrissa, A. Shisheva, Mammalian cell morphology and endocytic membrane homeostasis require enzymatically active phosphoinositide 5-kinase PIKfyve. *J. Biol. Chem.* **276**, 26141–26147 (2001).
13. A. C. Rutherford *et al.*, The mammalian phosphatidylinositol 3-phosphate 5-kinase (PIKfyve) regulates endosome-to-TGN retrograde transport. *J. Cell Sci.* **119**, 3944–3957 (2006).
14. D. Sbrissa *et al.*, Core protein machinery for mammalian phosphatidylinositol 3,5-bisphosphate synthesis and turnover that regulates the progression of endosomal transport. Novel Sac phosphatase joins the ArPIKfyve-PIKfyve complex. *J. Biol. Chem.* **282**, 23878–23891 (2007).
15. O. C. Ikonomov *et al.*, Functional dissection of lipid and protein kinase signals of PIKfyve reveals the role of PtdIns 3,5-P<sub>2</sub> production for endomembrane integrity. *J. Biol. Chem.* **277**, 9206–9211 (2002).
16. H. B. J. Jefferies *et al.*, A selective PIKfyve inhibitor blocks PtdIns(3,5)P<sub>2</sub> production and disrupts endomembrane transport and retroviral budding. *EMBO Rep.* **9**, 164–170 (2008).
17. O. Sano *et al.*, Vacuolin-1 inhibits autophagy by impairing lysosomal maturation via PIKfyve inhibition. *FEBS Lett.* **590**, 1576–1585 (2016).
18. J. Cerny *et al.*, The small chemical vacuolin-1 inhibits Ca<sup>2+</sup>-dependent lysosomal exocytosis but not cell resealing. *EMBO Rep.* **5**, 883–888 (2004).
19. X. Cai *et al.*, PIKfyve, a class III PI kinase, is the target of the small molecular IL-12/IL-23 inhibitor apilimod and a player in Toll-like receptor signaling. *Chem. Biol.* **20**, 912–921 (2013).
20. G. Sharma *et al.*, A family of PIKfyve inhibitors with therapeutic potential against autophagy-dependent cancer cells disrupt multiple events in lysosome homeostasis. *Autophagy* **15**, 1694–1718 (2019).
21. O. C. Ikonomov *et al.*, Active PIKfyve associates with and promotes the membrane attachment of the late endosome-to-trans-Golgi network transport factor Rab9 effector p40. *J. Biol. Chem.* **278**, 50863–50871 (2003).
22. C. Chen *et al.*, Identification of novel vacuolin-1 analogues as autophagy inhibitors by virtual drug screening and chemical synthesis. *Molecules* **22**, 891 (2017).
23. Y. Lu *et al.*, Vacuolin-1 potently and reversibly inhibits autophagosome-lysosome fusion by activating RAB5A. *Autophagy* **10**, 1895–1905 (2014).
24. B. E. Sands *et al.*, Randomized, double-blind, placebo-controlled trial of the oral interleukin-12/23 inhibitor apilimod mesylate for treatment of active Crohn's disease. *Inflamm. Bowel Dis.* **16**, 1209–1218 (2010).
25. Y. Wada *et al.*, Apilimod inhibits the production of IL-12 and IL-23 and reduces dendritic cell infiltration in psoriasis. *PLoS One* **7**, e35069 (2012).
26. E. A. Nelson *et al.*, The phosphatidylinositol-3-phosphate 5-kinase inhibitor apilimod blocks filoviral entry and infection. *PLoS Negl. Trop. Dis.* **11**, e0005540 (2017).
27. S. Qiu *et al.*, Ebola virus requires phosphatidylinositol (3,5) bisphosphate production for efficient viral entry. *Virology* **513**, 17–28 (2018).
28. J. S. Spence, T. B. Krause, E. Mittler, R. K. Jangra, K. Chandran, Direct visualization of Ebola virus fusion triggering in the endocytic pathway. *mBio* **7**, e01857-15 (2016).
29. R. Burakoff *et al.*, A phase 1/2A trial of STA 5326, an oral interleukin-12/23 inhibitor, in patients with active moderate to severe Crohn's disease. *Inflamm. Bowel Dis.* **12**, 558–565 (2006).

30. S. Krausz *et al.*, Brief report: A phase IIa, randomized, double-blind, placebo-controlled trial of apilimod mesylate, an interleukin-12/interleukin-23 inhibitor, in patients with rheumatoid arthritis. *Arthritis Rheum.* **64**, 1750–1755 (2012).
31. C. E. Hulseberg *et al.*, Arbidol and other low-molecular-weight drugs that inhibit Lassa and Ebola viruses. *J. Virol.* **93**, 11 (2019).
32. J. Dyall *et al.*, Identification of combinations of approved drugs with synergistic activity against Ebola virus in cell cultures. *J. Infect. Dis.* **218** (suppl. 5), S672–S678 (2018).
33. R. Bago *et al.*, Characterization of VPS34-IN1, a selective inhibitor of Vps34, reveals that the phosphatidylinositol 3-phosphate-binding SGK3 protein kinase is a downstream target of class III phosphoinositide 3-kinase. *Biochem. J.* **463**, 413–427 (2014).
34. I. Glowacka *et al.*, Evidence that TMPRSS2 activates the severe acute respiratory syndrome coronavirus spike protein for membrane fusion and reduces viral control by the humoral immune response. *J. Virol.* **85**, 4122–4134 (2011).
35. A. Shulla *et al.*, A transmembrane serine protease is linked to the severe acute respiratory syndrome coronavirus receptor and activates virus entry. *J. Virol.* **85**, 873–882 (2011).
36. S. Matsuyama *et al.*, Efficient activation of the severe acute respiratory syndrome coronavirus spike protein by the transmembrane protease TMPRSS2. *J. Virol.* **84**, 12658–12664 (2010).
37. M. Hoffmann *et al.*, SARS-CoV-2 cell entry depends on ACE2 and TMPRSS2 and is blocked by a clinically proven protease inhibitor. *Cell* **181**, 271–280.e8 (2020).
38. G. Simmons *et al.*, Characterization of severe acute respiratory syndrome-associated coronavirus (SARS-CoV) spike glycoprotein-mediated viral entry. *Proc. Natl. Acad. Sci. U.S.A.* **101**, 4240–4245 (2004).
39. S. Gayle *et al.*, Identification of apilimod as a first-in-class PIKfyve kinase inhibitor for treatment of B-cell non-Hodgkin lymphoma. *Blood* **129**, 1768–1778 (2017).
40. C. D. S. Nelson, A. Derdowski, M. S. Maginnis, B. A. O'Hara, W. J. Atwood, The VP1 subunit of JC polyomavirus recapitulates early events in viral trafficking and is a novel tool to study polyomavirus entry. *Virology* **428**, 30–40 (2012).
41. M. V. Baranov *et al.*, The phosphoinositide kinase PIKfyve promotes cathepsin-S-mediated major histocompatibility complex class II antigen presentation. *iScience* **11**, 160–177 (2019).
42. M. Côté *et al.*, Small molecule inhibitors reveal Niemann-Pick C1 is essential for Ebola virus infection. *Nature* **477**, 344–348 (2011).
43. I. Le Blanc *et al.*, Endosome-to-cytosol transport of viral nucleocapsids. *Nat. Cell Biol.* **7**, 653–664 (2005).
44. Y. Zhou *et al.*, Protease inhibitors targeting coronavirus and filovirus entry. *Antiviral Res.* **116**, 76–84 (2015).
45. T. K. Soh, S. P. J. Whelan, Tracking the fate of genetically distinct vesicular stomatitis virus matrix proteins highlights the role for late domains in assembly. *J. Virol.* **89**, 11750–11760 (2015). Erratum in: *J. Virol.* **90**, 5847 (2016).
46. S. Piccinotti, T. Kirchhausen, S. P. J. Whelan, Uptake of rabies virus into epithelial cells by clathrin-mediated endocytosis depends upon actin. *J. Virol.* **87**, 11637–11647 (2013).
47. A. C. Wong, R. G. Sandesara, N. Mulherkar, S. P. Whelan, K. Chandran, A forward genetic strategy reveals destabilizing mutations in the Ebolavirus glycoprotein that alter its protease dependence during cell entry. *J. Virol.* **84**, 163–175 (2010).
48. S. P. Whelan, L. A. Ball, J. N. Barr, G. T. Wertz, Efficient recovery of infectious vesicular stomatitis virus entirely from cDNA clones. *Proc. Natl. Acad. Sci. U.S.A.* **92**, 8388–8392 (1995).
49. F. A. Ran *et al.*, Genome engineering using the CRISPR-Cas9 system. *Nat. Protoc.* **8**, 2281–2308 (2013).
50. Y.-Y. Chou *et al.*, Identification and characterization of a novel broad spectrum virus entry inhibitor. *J. Virol.* **90**, 4494–4510 (2016).
51. M. Yuan *et al.*, A highly conserved cryptic epitope in the receptor-binding domains of SARS-CoV-2 and SARS-CoV. *Science* **368**, 630–633 (2020).
52. E. Cocucci, F. Aguet, S. Boulant, T. Kirchhausen, The first five seconds in the life of a clathrin-coated pit. *Cell* **150**, 495–507 (2012).